Transient mold fluid flow with well- and mountain- bottom nozzles in continuous casting of steel

R. Chaudhary[a], Go-Gi Lee[b], B. G. Thomas[a], Seon-Hyo Kim[b]
[,a]Department of Mechanical Science and Engineering, University of Illinois at Urbana-Champaign
1206 W. Green St., Urbana, IL, USA, 61801
[b]Department of Materials Science and Engineering, Pohang University of Science and Technology, Pohang, Kyungbuk, 790-784, South Korea

Abstract:

Nozzle shape plays a key role in determining the flow pattern in the mold of the continuous casting process under both steady-state and transient conditions. This work applies computational models and experiments with a 1/3rd-scale water model to characterize flow in the nozzle and mold to evaluate well-bottom and mountain-bottom nozzle performance. Velocities predicted with the three-dimensional k-ε turbulence model agree with both particle image velocimetry and impeller measurements in the water model. The steady-state jet velocity and angle leaving the ports is similar for the two nozzle bottom designs. However, the results show that nozzles with a mountain-shaped bottom are more susceptible to problems from asymmetric flow, low-frequency surface flow variations, and excessive surface velocities. The same benefits of the well-bottom nozzle are predicted for flow in the steel caster.

Key Words:

Nozzle bottom, water model, PIV, asymmetry, time variations, computational model, k-epsilon, turbulence

I. Introduction

Both the steady-state flow pattern and transient variations in the mold cavity are important to steel quality in continuous casting. Excessive meniscus velocities and surface turbulence lead to inclusion defects due to slag entrainment and level fluctuations in the mold [1, 2]. Insufficient surface flows lead to meniscus freezing and other surface

defects [1, 2]. The mold flow pattern should be optimized to achieve a flat surface profile with stable meniscus velocities of the desired magnitude and minimum turbulence.

These important flow parameters are governed by the flow control system (stopper rod or slide gate), nozzle geometry, Submerged Entry Nozzle (SEN) depth, casting speed, strand cross-section dimensions, argon gas injection rate, slag behavior, and the application of electromagnetics [1]. The most influential and easily-changed of these parameters are the nozzle port geometry details (port angle, port area), and the nozzle bottom shape. In particular, the shape of nozzle bottom has an important influence on flow quality in the mold, including the surface velocity, surface level profile, and turbulent variations that vary the frequency and magnitude of their fluctuations and asymmetries. This paper applies computational model and water-model experiments to analyze and compare the effect of two popular nozzle bottom shapes on these flows.

II. Previous Work

Owing to the difficulty of plant experiments and the similar kinematic viscosity of water and steel, much previous insight into mold fluid flow has been gained using water models [1-6] Although most studies have focused on steady-state flow patterns, a few studies have noted transient phenomena [3-11]. Honeyands and Herberton [8] observed surface level fluctuations in a thin-slab water model with a characteristic frequency that increased with casting speed, according to the time period for flow to circulate around the mold cavity. Gupta and Lahiri [5] observed flow asymmetries in the lower recirculation zones that alternated between sides like large-scale vortex shedding. Lawson and Davidson [9] used Laser Doppler Velocimetry (LDV) to measure oscillatory flow in a 0.33-scale thin-slab water model. Low frequency oscillation modes had the most oscillatory energy, especially below 5Hz in the jets, and below 0.2Hz in the mold overall. This is consistent with findings of Sivaramakrishnan et al [11] and Assar et al [3] from velocities measured in a 0.4-scale water model using Particle Image Velocimetry (PIV).

Many previous computational models have been applied to predict fluid flow exiting the nozzle [12-15]. Many researchers have shown that computational predictions of steady k-ε based Reynolds-Averaged Navier-Stokes (RANS) models [12-14, 16-18] can reasonably predict the steady flow pattern measured in water models. Such models have been applied to investigate the effect of port angle and port shape on flow pattern and jet characteristics exiting the nozzle port [12, 15]. Bai et al [13,14] extended such a model to include multiphase effects and asymmetries from the slide-gate orientation [12] to investigate the effect of gas injection, casting speed, gate opening, bubble size, port angle and port shape [13]. Nozzle bottom was not found to have much effect on the steady flow pattern. However, optimizing the steady-flow pattern is not as important as avoiding defects due to turbulent flow effects such as transient level fluctuations.

Several recent models have been developed to study transient flow phenomena in the mold. Huang and Thomas [17] showed that an unsteady RANS model could simulate flow evolution in a caster and steel-slag interface level fluctuations induced by sudden changes of nozzle inlet conditions. Others have applied Large Eddy Simulation (LES) [11, 18-21] and showed it to match the time-average flow pattern measured in both water models [11, 18-21] and in the steel caster with electromagnetic sensors [21]. Complex time-varying flow structures have been observed in the LES simulation results, [19, 20] even during nominally steady casting conditions. The velocity variations due to turbulence were compared with measurement. In spite of its known importance, few parametric studies have considered transient flow variations. The effect of nozzle bottom shape remains unclear, so is the subject of this work.

III. Water model experiments

A 1/3rd - scale water model was constructed to measure jet and surface velocities using both PIV and impeller velocity meters. Vertical movement of a centered (aligned) stopper rod controls the flow rate through an annular space of ~2 mm minimum thickness. Water flows down the nozzle and into the mold through bifurcated ports angled 25 degree downward. Fig-1 shows the geometry in front view (right) and side view (left). Water

exits the bottom of the water-model mold through 11 outlets of 25 mm diameter. From there, water passes through a flow meter to the water storage bath. Water is then pumped back up to the tundish through a second flow meter, which is used by the stopper-rod control system to maintain constant flow rate. Table-1 provides details of the dimensions and casting conditions of the water model and the corresponding full-scale steel caster.

Fig-2 (a) shows the nozzle geometry with the well-shaped bottom. As typical, the ports are oversized with total port-to-bore ratio of 2.8. Fig-2 (b) and Fig-2(c) show close-ups of the well-bottom and mountain-bottom shapes. Both nozzles otherwise have the same geometry.

Velocity was measured using PIV just below the ports at the centerline plane of the mold for the well-bottom nozzle. A 2 mm hick plane was illuminated using laser light, and velocity vectors were computed by digital analysis of snapshots taken 0.6 ms apart. These velocities were measured every 0.14 s at each of the 125 x 56 grid of points in the 285-mm wide and 130-mm high measurement window and time-averaged over 360 seconds.

Velocities were also measured using impeller velocity probes. Time-varying data was collected at a frequency of 1 Hz. Fig-3 shows the location and orientation of each sensor probe. Each probe is a 35mm long open-ended tube (22mm inner and 28 mm outer diameter) containing a small propeller that rotates in proportion with water speed. Jet velocities were measured by touching the probe to the port bottom and aligning it with the port angle (25 degree down). Surface velocity was recorded 60 mm from each narrow face and 25 mm below the top free surface in the mold for both nozzles. The impeller velocity probes have a total response time of ~ 10s (i.e. 0.1 Hz), including electrical response time (~0.4s to reach 63% of end value) and mechanical response time (for the vanes to respond to increase or decrease in flow). The probes are accurate over the velocity range of 0.02-5 m/s. For each case, mean velocities were averaged over 2000s (except 1000s for mountain-surface) and corresponding isotropic turbulent kinetic energies were derived using standard root-mean square [22], assuming unmeasured

components had the same variations. Finally, power spectra were calculated using the Mean Squared Amplitude (MSA) formulation [19].

IV. Computational model

A computational model has been formulated to simulate time-averaged turbulent fluid flow in the nozzles and molds of well and mountain bottom nozzles. The steady-state, 3-dimensional, incompressible, Navier-Stokes equations for momentum conservation are solved with the continuity equation, and the standard k and ε equations to model turbulence (Launder and Spalding [23]) are given by [24]. This approach needs a less-refined mesh, so is faster than the Direct Numerical Simulation (DNS) and LES methods, which are more accurate for transient flow.

The model domain contains only the liquid pool, so naturally has straight walls for the water model. When modeling the steel caster, the domain has curved walls to match the shape of the solidification front, which was calculated using CON1D [25]. In addition to standard no-slip wall laws used on all solid boundaries [22], downward velocity at the solidification front was fixed at the casting speed. To account for shell solidification, a source term of mass-sink per unit volume is added to the continuity equation as follows [26-27]:

$$\rho\left(\nabla \bullet \vec{v}\right) = S_{mass} = -\frac{\rho V_{casting} A}{V} \qquad (1)$$

Where ρ is the density of the fluid (kg/m^3), $V_{casting}$ is the casting speed, A is the projection area in casting direction and V is the volume of the sink cells, which are 1-mm thick and extend over the domain walls boundaries that represent the solidification front. A corresponding sink term for the momentum extracted per unit volume into the shell is added to each of the three (x-, y- and z-) momentum equations:

$$\vec{S}_{mom} = -\frac{\rho V_{casting} A}{V}\vec{v} \qquad (2)$$

These terms were implemented with a User-Defined Function (UDF) C-language subroutine in FLUENT [28]. More details on these sinks terms are given by Creech (1999) and Rietow (2007) [26-27].

Assuming symmetrical flow, 2-fold symmetry of the geometry enables a model of only quarter of the nozzle and strand, to minimize computation. The nozzle and strand are discretized using about 19,000 and 0.136 Million hexahedral cells respectively as shown in Fig-4. To better model flow entering the stopper region, a cylindrical portion of the tundish bottom (with 200 mm diameter and 150 mm height), is created around the top of the SEN. Fig-5 gives close-up views and meshes of the stopper and bottom regions of both nozzles. Average velocity with small values of k- and ε- (10^{-5} m^2/s^2, 10^{-5} m^2/s^3) were fixed at the circumference and top annular regions of the cylinder to match the flow rate for typical casting speed and dimensions (Table-1).

To improve efficiency, nozzle flow is simulated first, using pressure outlet boundary conditions. The velocities, turbulent kinetic energy and dissipation rate at the outlet plane from the nozzle ports are then used as boundary conditions for the inlet surface to the strand. Hershey et al [14] showed that this approach matches well with results of simulations that combine the nozzle and strand together. Convergence is easier because residuals in the important low-velocity regions of the strand are not overly influenced by small errors in the high velocities inside the nozzle. The meshes of the nozzle outlet and the strand inlet were identical with one-to-one mapping in order to ensure accurate flux balance between the two computational domains.

Free-slip boundaries with zero normal velocity were employed at the top free surface, and level fluctuations were calculated using pressure distribution along the free surface based upon potential energy conservation [17, 29]. Pressure outlet boundary conditions were also used at strand exit. In case of reverse flow entering the lower recirculation zone, small values of k- and ε- (10^{-5} m^2/s^2, $10^{-5}m^2/s^3$) were set at the strand domain exit, along with 0 Pa gauge pressure.

The equations for the three momentum components, k-, and ε- are discretized using the Finite Volume method in FLUENT [28] with 1st -order upwind schemes for convection terms, including Poisson's equation for pressure correction. These discretized equations are then solved for velocity and pressure using the Semi-Implicit Pressure Linked Equations (SIMPLE) algorithm, starting with initial conditions of zero velocity [29]. Standard wall laws were used as boundary conditions [30]. Finally, k- and ε- equations are solved. The turbulent viscosity field is obtained from k and ε and added to the molecular viscosity to obtain effective viscosity for the next step update. The segregated solver in FLUENT was used to solve all equations. In all simulations, convergence was defined when all scaled residuals were reduced below 10^{-4}. All computations were performed on a PC with a 2.66 GHz Intel® Xeon processor and 4.0 GB RAM. Each nozzle simulation converged in about 15 minutes and required around 1000 iterations. Strand simulations took around 3 hours with 7600 iterations for the mountain-bottom nozzle and about 2 hours with 4000 iterations for the well-bottom nozzle.

V. Model Validation

The computational model predictions are validated here by comparing with the time-averaged PIV, impeller velocity and turbulence measurements. Fig-6(a) shows the PIV measurement window, which extends down from the port bottom and Fig-6(b) shows the average velocity magnitude contours. The bottom of the SEN extends into the top of the frame. The maximum velocity is 1.022 m/s on the upper left side. On the upper right side, shadow effects from the nozzle spoil the PIV measurements in the red-triangle region.

Fig-6(c) and Fig-6(d) gives velocity contours modeled using 2nd order and 1st order up-wind convection schemes respectively. With 2nd order upwinding, Fig-6(c), the maximum velocity is 1.09 m/s and the jet is thinner, bending upward slightly. The jet shape

matches most closely with the PIV measurements. With 1st-order upwinding, Fig-6(d), numerical diffusion makes the jet thicker and more stable, and the maximum speed drops to 1.02 m/s. These results match closer to the measured jet velocity, and with the shape of the flow pattern deeper in the caster. Moreover, the 2nd order scheme is less stable and did not converge for the mountain-bottom nozzle. Thus, the 1st order scheme was used in further simulations.

A comparison of impeller measurements of velocity and turbulence with computational model predictions is summarized in Table-2. The velocity predictions agree with the time-average of the measurements about as well as the measurements on the right and left sides agree with each other. Moreover, the trends are consistent. The well-bottom nozzle velocity measurements show little variation between sides, and agree with the predictions within 1%. The mountain-bottom nozzle exhibits significant asymmetry between left and right, indicating that the time-averaging period was too short for this nozzle. The predictions agree within these variations. For example, surface velocity averaged over the last 500s is 0.180m/s, which matches exactly with the prediction.

Agreement with the turbulent kinetic energy measurements is not quite as good. The measured turbulence of the jet exiting the ports is five orders of magnitude smaller than at the surface. This is contrary to expectations that the jet should be more turbulent, as predicted with the computational model. This is believed to be due to the known inability of the impeller probe to respond to the high-frequency fluctuations that dominate the jet turbulence, due to the inertia of the impeller. In addition, the fixed orientation of the probe is unable to measure non-axial fluctuations, which were observed to be significant in this region. Agreement is much better at the top surface, which has lower-frequency fluctuations. Measurements and predictions agree reasonably for the mountain-bottom nozzle, and are in the same range for the well-bottom nozzle. Moreover, the trends agree. Thus, the model predictions and measurements are used together to understand flow in the remainder of this work.

VI. Computational Results

A. Nozzle Flow

Fig-7 gives the velocity contours and vectors near the stopper rod head and bottom region of both nozzles. The maximum velocity is 3.8 m/s and is found in the thinnest part of the annular region between the stopper rod and the tundish bottom. Fig-8 compares streamlines and Table-3 quantifies the jet characteristics for both nozzles. The jet in the well-bottom nozzle is more diffusive and thicker with a smaller back flow zone (27% vs. 30% in mountain bottom). In the mountain-bottom nozzle, flow goes straight along the side of the mountain with high velocity, producing a thinner and less diffusive jet with smaller horizontal and vertical jet angles.

Fig-9 compares velocity contours and vectors at port exit. Secondary flows from the mountain bottom nozzle are weaker, as flow is directed more towards the narrow face. Fig-10 gives velocity contours and vectors on lines angled 25 degrees from the port bottom in the mold region close to SEN. The maximum velocity is close to the port bottom in both ports with a steeper, thicker jet (also seen in Fig-7 and Table-3) from the well-bottom nozzle. Higher outward, downward and horizontal weighted-average jet velocities exiting the mountain bottom nozzle are observed in both the experiments and computations. Turbulent kinetic energy is much higher in the well-bottom nozzle, with higher frequency fluctuations causing a more dissipative jet.

B. Mold Flow Pattern

Fig-11 presents the mold flow patterns at the mid-plane between wide faces for both nozzles. The higher dissipation rate leaving the port of the well-bottom nozzle causes the jet turbulent kinetic energy to decrease more as it moves through the mold. This thicker and more diffusive jet thus loses its momentum faster as it splits into upper and lower recirculation zones with weaker flow along the narrow face. Maximum velocity is found near the bottom of port exit, and is 1.23 m/s with the well-bottom nozzle. With the

mountain-bottom nozzle, the jet is faster (1.31 m/s) which leads to higher surface velocity. The latter jet also bends upwards more as it crosses the mold, further contributing towards the higher surface velocity. Also, the lower recirculation zone is predicted to break up into more complex flow structures.

Fig-12 gives the vertical speed along the mid-plane vertical line at 10 mm from narrow face. The mountain-bottom nozzle has faster flow in the upper recirculation zone. The jet impinges the narrow face at 180 mm below the top free surface with both nozzles. The free surface level for both nozzles is given in Fig-13 at the mid-plane between wide faces. The surface is raised near the narrow face and SEN, as common with a double-roll flow pattern. The mountain-bottom nozzle gives around 2.5 times higher surface waves, owing to its ~1.5 times higher horizontal surface velocity, as shown in Fig-14 (a). This higher surface velocity agrees with the measurements, (Fig. 16) and is due to the stronger flow up the narrow face,

The turbulent kinetic energies predicted for the two nozzles at the free surface are given in Fig-14 (b). The mountain-bottom nozzle gives ~5 times higher turbulent kinetic energy compared to the well-bottom. This is due to the low frequency and high magnitude fluctuations in the surface velocity for this nozzle.

VII. Water Model Results

A. Jet Velocity

Fig-15 shows the jet velocities measured on the left and right sides with the impeller probe. Time-averaged jet velocities with the well-bottom nozzle are ~0.686 m/s and are quite symmetric, with the left and right sides matching within ~0.3% over 2000s. In the mountain bottom nozzle, the corresponding jet velocities average 0.950 m/s, which is significantly higher. They are also less symmetric with ~1.4% higher velocity on the left side, which indicates stronger, lower-frequency variations.

B. Surface Velocity

Fig-16 shows the measured histories of the horizontal velocities near the surface near the left and right side of the mold for both nozzles, along with the their time averaged values. For the well bottom nozzle, time-averaged horizontal surface velocities are ~0.109 m/s, with the right side 11.6% higher than the left. The mountain-bottom nozzle has more than 50% higher average surface velocities, 0.157 m/s, due to the higher jet velocity. Its asymmetry is also higher, with 12.1% higher velocity on the right side. Relative to the jet, these surface flow results show that asymmetry increases as the flow travels through the mold. Furthermore, the mountain-bottom nozzle is more susceptible to asymmetric flow.

C. Velocity Fluctuations

Power spectrums of the jet and surface velocity fluctuations of both nozzles can be seen in Fig-17 and Fig-18 respectively. Due to ~10s response time of the impeller probe, only energies for frequencies up to 0.1 Hz are plotted. In all cases, most of the energy is found in low frequencies. The general drop in energy observed with increasing frequency matches previous work [10, 15]. An exception is the small peak found at ~0.07 Hz (~14s). The same frequencies dominate in the jet and surface for both nozzles. Energy in the jet is higher in the well-bottom nozzle, especially at frequencies above 0.01 Hz. This is due to strong recirculation observed in the bottom of the nozzle (Fig-8). The mountain nozzle deflects the jet smoothly towards the ports (Fig-8), slicing through the flow like a knife-edge. This allows the jets to retain more of their momentum, but with less turbulence. This causes the trend in energy spectrum at the surface to reverse. The mountain-bottom nozzle experiences much greater surface velocity fluctuations. Fig. 18 shows the increase to be more than an order of magnitude at frequencies ranging from 0.002 – 0.035 Hz, which corresponds with time periods of 33-500 s. This finding is also seen in Fig-16. The well bottom nozzle has energy distributed over a wider frequency range in both jet and surface velocities.

D. Mechanism

The increased velocity fluctuations and left-right asymmetry of the mountain-bottom nozzle are explained with Fig-19. Transient variations in nozzle flow may send higher

velocity down one side of the nozzle. The mountain bottom slices the flow, sending this higher velocity flow directly out the adjacent port. The well bottom, on the other hand, mixes the flow so the jets exiting the ports are less sensitive to asymmetries.

VII. Comparison of water model with full-scale steel caster

Simulations of a full-scale steel caster with well-bottom nozzle were performed to evaluate the water model findings. The laboratory water model has several differences from the real caster: **1.** Geometric scaling of all linear dimensions to 1/3rd, **2.** No solidifying shell and stationary walls, **3.** A domain bottom with water exiting through circular holes in a horizontal plate instead of a very long, gradually-tapering flow domain. **4.** Air above the free surface instead of powder, sintered and liquid slag layers. A steel caster was simulated with and without the solidifying shell for conditions in Table-1. Fig-20 gives the shell thickness profiles down the wide and narrow faces calculated using CON1D [25].

Fig-21 presents the velocity contours and streamlines at the mid-plane between wide faces in the steel caster with the solidifying shell. The casting speed for the full-scale caster matches the Froude number of 0.005 of the water model. The flow pattern is generally similar to the water model. Comparison of horizontal surface velocity between water model (after converting to full scale), and the steel caster is given in Fig-22. The horizontal axis is non-dimensionalized to compare both water model and caster. The vertical axis is simply the horizontal velocity for the steel caster. Horizontal velocity for the water model was multiplied by 1.732, (the square root of the length scale of 3) according to the Froude criterion. The horizontal velocity in the water model falls in between the caster velocities with and without the solidifying shell. Note that flow in the water model is in the transition regime (Re=2200 based on strand hydraulic diameter) while the steel caster is fully turbulent (Re=13500). The water model velocities would match the caster without the shell if it was fully turbulent..

The maximum surface velocity predicted in the real full-scale steel caster with the well-bottom nozzle is ~0.3 m/s, which is in the safe operating window of 0.2-0.4 m/s, [2]. Maximum surface velocity with the mountain-bottom nozzle is predicted to be ~0.5 m/s, which is above the upper limit suggested by Kubota [2] to avoid flow problems such as slag entrainment. Thus, the well-bottom nozzle is preferred over the mountain-bottom nozzle for this steel caster and conditions. If casting conditions produced very small surface velocities, then the mountain-bottom nozzle might appear to be better. However, the results of this work suggest that changing the flow pattern in some other way and using the well-bottom nozzle is the best solution.

The free-surface level profile comparison between water model and steel caster is given in Fig-23. The free surface level without shell and air above matches most closely with water model, as expected, although the water model underpredicts by a factor of 2.3. Introducing the shell and adding slag both increase the profile variations. Thus, the water model underpredicts surface level variations in the caster using Froude scaling.

VIII. Summary

This work investigates well-bottom and mountain-bottom type nozzles both experimentally and numerically. The computational model agrees very well with measured velocities in all cases, but overpredicts turbulent kinetic energy in the jet and surface of the well bottom nozzle perhaps due to time resolution (~0.1 Hz) of the impeller probe and fluctuations being higher frequency. The measured surface turbulence in mountain bottom nozzle matches well with the simulations. Based upon experiments and the validated computational model, the following conclusions have been drawn, and are summarized in Table-4:

1. The jet from the well-bottom nozzle is thicker, steeper-downward and more diffusive, with higher turbulent kinetic energy and dissipation rate, relative to the mountain bottom nozzle jet.
2. The mountain-bottom nozzle produces a thinner jet with stronger, lower-frequency fluctuations, making it more asymmetrical in short-term time averages.

3. Velocity fluctuations decrease in frequency from the jet leaving the ports to the surface in both nozzles.
4. The mountain-bottom nozzle produces ~50% higher surface velocity in the mold.
5. The mountain-bottom nozzle causes surface velocity fluctuations with almost 96% of total measured energy at lower frequencies (33-500s time periods).
6. The higher velocity and turbulence at the surface causes higher variation in surface level profile, more level fluctuations, and easier slag entrainment with the mountain-bottom nozzle.
7. Full scale steel casters have proportionally higher speed, including higher surface velocities, and level fluctuations, which are reasonably characterized by Froude similarity. The above water-model findings are predicted to hold in the steel caster as well.
8. With less surface fluctuations, the well-bottom nozzle is recommended over the mountain-bottom shape for steel quality.

Acknowledgements

The authors thank Young-Jin Jeon and Prof. Hyung-Jin Sung, Dept. of Mechanical Eng., KAIST, South Korea, and Seong-Mook Cho, POSTECH, South Korea for help with the PIV measurements. They also thank POSCO and Oh-Duck Kwon, Shin-Eon Kang, POSCO Technical Research Laboratories for relevant data and providing the water model and ANSYS Inc. for supplying FLUENT. Support from the Continuous Casting Consortium, University of Illinois at Urbana-Champaign, POSCO, South Korea (Grant No. 4.0002397.01) and the National Science Foundation (Grant No. DMI 05-00453) is gratefully acknowledged.

References

1. B. G. Thomas, *Chapter 14. Fluid Flow in the mold*, in *Making, Shaping and Treating of Steel*, A.W. Cramb, Editor. 2003, AISE Steel Foundation: Pittsburgh, PA.
2. J. Kubota, et al. *Meniscus Flow Control in the Mold by Travelling Magnetic Field for High Speed Slab Caster*. in *Steelmaking Conf. Proceedings*. 1991.
3. M. B. Assar, P. H. Dauby, and G.D. Lawson, *Opening the Black Box: PIV and MFC Measurements in a Continuous Caster Mold*, in *Steelmaking Conf. Proc.* 2000, ISS, Warrendale, PA: Pittsburgh, PA. p. 397-411.
4. D. Gupta and A. K. Lahiri, *A water model study of the flow asymmetry inside a continuous slab casting mold.* Metallurgical and Materials Transactions B-Process Metallurgy and Materials Processing Science, 1996. **27**(5): p. 757-764.
5. D. Gupta and A. K. Lahiri, *Water modeling study of the jet characteristics in a continuous casting mold.* Steel Research, 1992. **63**(5): p. 201-204.
6. B. G. Thomas, X. Huang, and R. C. Sussman, *Simulation of Argon Gas Flow Effects in a Continuous Slab Caster.* Metall. Trans. B, 1994. **25B**(4): p. 527-547.
7. B. G. Thomas and L. Zhang, *Mathematical modeling of fluid flow in continuous casting.* ISIJ International, 2001. **41**(10): p. 1181-1193.
8. T. Honeyands and J. Herbertson, *Flow Dynamics in Thin Slab Caster Moulds.* Steel Research, 1995. **66**(7): p. 287-293.
9. N. J. Lawson and M. R. Davidson, *Oscillatory flow in a physical model of a thin slab casting mould with a bifurcated submerged entry nozzle.* Journal of Fluids Engineering-Transactions of the Asme, 2002. **124**(2): p. 535-543.
10. Dong Xu, William K. Jones, and James W. Evans, *PIV Physical Modeling of Fluid Flow in the Mold of Continuous Casting of Steel*, in *Processing of Metals and Advanced Materials: Modeling, Deisgn and Properties*, B.Q. Li, Editor. 1998, TMS, Warrendale, PA: San Antonio, TX. p. 3-14.
11. S. Sivaramakrishnan, B. G. Thomas, and S. P. Vanka, *Large Eddy Simulation of Turbulent Flow in Continuous Casting of Steel*, in *Materials Processing in the Computer Age*, V. Voller and H. Henein, Editors. 2000, TMS, Warrendale, PA. p. 189-198.

12. H. Bai and B.G. Thomas, *Turbulent Flow of Liquid Steel and Argon Bubbles in Slide-Gate Tundish Nozzles: Part I. Model Development and Validation.* Metallurgical and Materials Transactions B, 2001. **32**(2): p. 253-267.
13. H. Bai and B.G. Thomas, *Turbulent Flow of Liquid Steel and Argon Bubbles in Slide-Gate Tundish Nozzles: Part II. Effect of Operation Conditions and Nozzle Design.* Metallurgical and Materials Transactions B, 2001. **32**(2): p. 269-284.
14. D. E. Hershey, B. G. Thomas, and F.M. Najjar, *Turbulent Flow through Bifurcated Nozzles.* Int. J. Num. Meth. in Fluids, 1993. **17**(1): p. 23-47.
15. F. M. Najjar, B. G. Thomas, and D. E. Hershey, *Numerical study of steady turbulent flow through bifurcated nozzles in continuous casting.* Metall. Mater. Trans. B, 1995. **26B**(4): p. 749-765.
16. B. G. Thomas, L. J. Mika, and F.M. Najjar, *Simulation of Fluid Flow Inside a Continuous Slab Casting Machine.* Metall. Trans. B, 1990. **21B**(2): p. 387-400.
17. X. Huang and B. G. Thomas, *Modeling of transient flow phenomena in continuous casting of steel.* Canadian Metallurgical Quarterly, 1998. **37**(3-4): p. 197-212.
18. K. Takatani, et al., *Mathematical model for transient fluid flow in a continuous casting mold.* ISIJ International, 2001. **41**(10): p. 1252-1261.
19. Q. Yuan, B.G. Thomas, and S.P. Vanka, *Study of Transient Flow and Particle Transport during Continuous Casting of Steel Slabs, Part 1. Fluid Flow.* Metal. & Material Trans. B., 2004. **35B**(4): p. 685-702.
20. Q. Yuan, et al., *Computational and Experimental Study of Turbulent Flow in a 0.4-Scale Water Model of a Continuous Steel Caster.* Metall. & Mater. Trans., 2004. **35B**(5): p. 967-982.
21. B. G. Thomas, et al., *Comparison of four methods to evaluate fluid velocities in a continuous slab casting mold.* ISIJ International, 2001. **41**(10): p. 1262-1271.
22. H. Versteeg and W. Malalasekra, *An Introduction to Computational Fluid Dynamics: The Finite Volume Method Approach*. 1995, Essex, England: Longman Scientific Technical.
23. B. E. Launder and D. B. Spalding, *Mathematical Models of Turbulence*. 1972: London Academic Press.

24. B. G. Thomas, *Chapter 5. Modeling of Continuous Casting*, in *Making, Shaping and Treating of Steel*, A.W. Cramb, Editor. 2003, AISE Steel Foundation: Pittsburgh, PA.
25. Y. A. Meng and B.G. Thomas, *Heat-transfer and solidification model of continuous slab casting: CON1D.* Metallurgical and Materials Transactions B, 2003. **34**(5): p. 685-705.
26. B. T. Rietow, *M.S. Thesis: Fluid Velocity Simulation and Measurement in Thin Slab Casting*, in *Mechanical and Industrial Engineering*. 2007, University of Illinois at Urbana-Champaign: Urbana.
27. D. Creech, *M.S. Thesis: Computational Modeling of Multiphase Turbulent Fluid Flow and Heat Transfer in the Continuous Slab Casting Mold*, in *Mechanical and Industrial Engineering*. 1999, University of Illinois at Urbana-Champaign: Urbana.
28. *FLUENT6.3-Manual*, I. ANSYS, Editor. 2007: Lebanon, NH.
29. G.A. Panaras, A. Theodorakakos, and G. Bergeles, *Numerical Investigation of the Free Surface in a continuous Steel Casting Mold Model.* Metall. Mater. Trans. B, 1998. **29B**(5): p. 1117-1126.
30. B. E. Launder and D. B. Spalding, *The numerical computation of turbulent flows.* Computer Methods in Applied Mechanics and Engineering, 1974. **3**(2): p. 269-289.

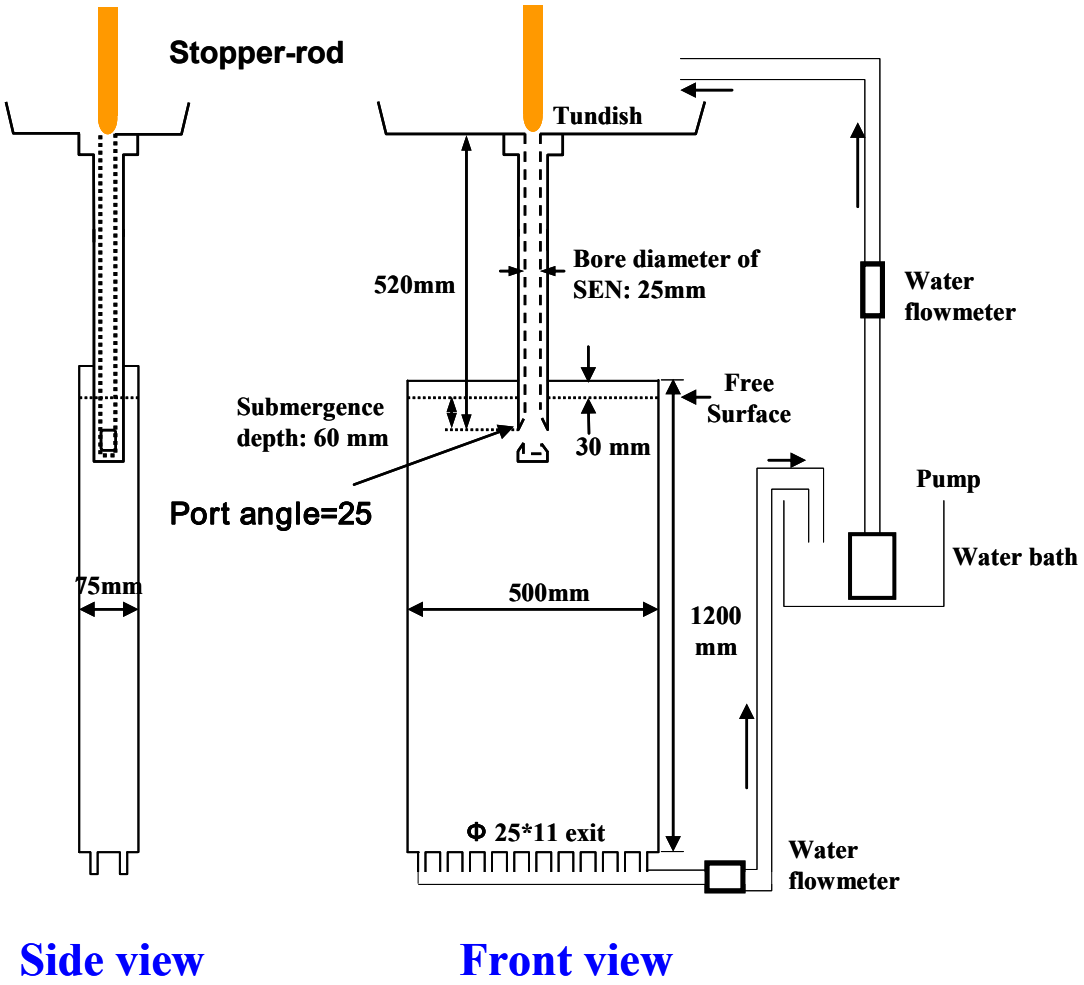

Fig-1 Dimensions of 1/3rd-scale water model with well-bottom nozzle

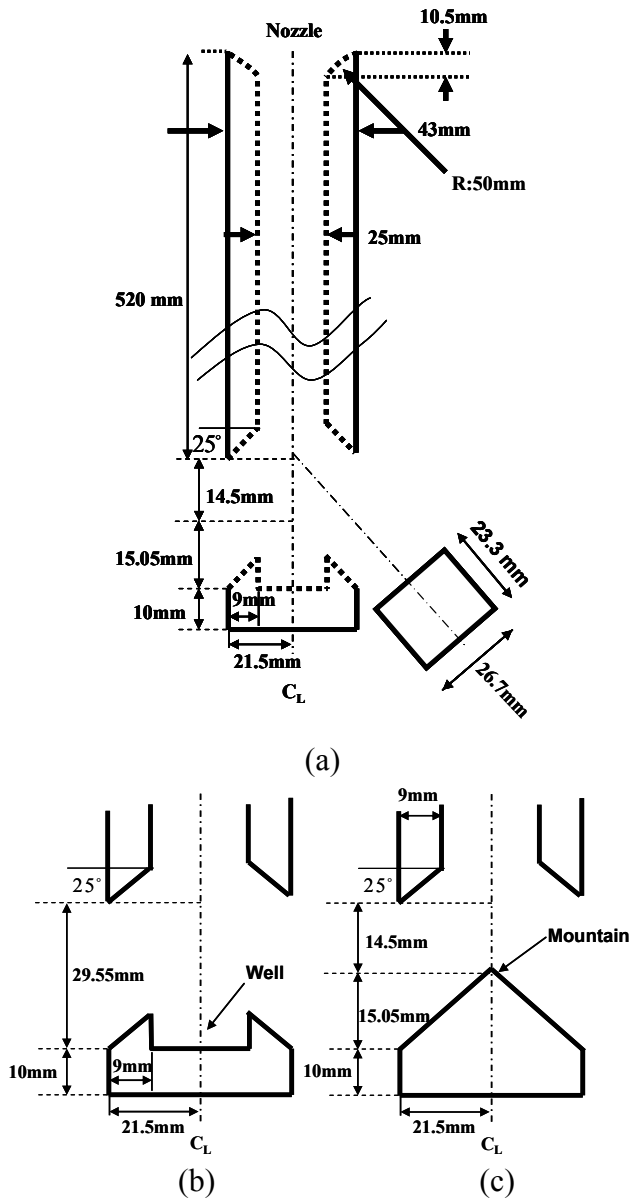

Fig-2 Geometry of (a) nozzle and close-up of: (b) well-bottom and (c) mountain bottom shapes

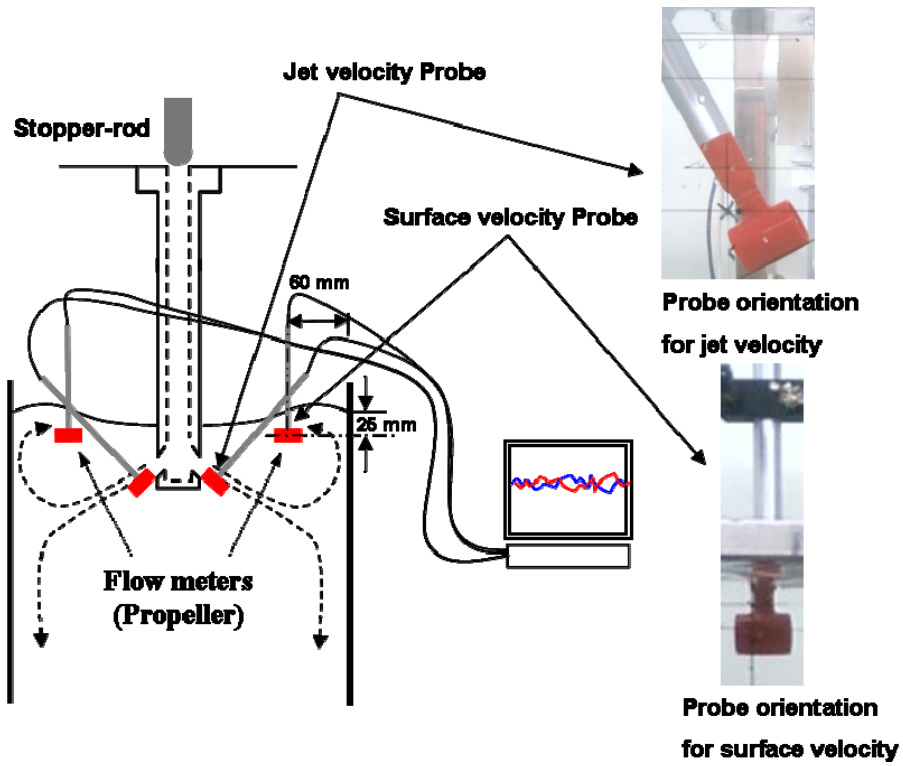

Fig-3 Schematic of the impeller velocity probe locations and orientations

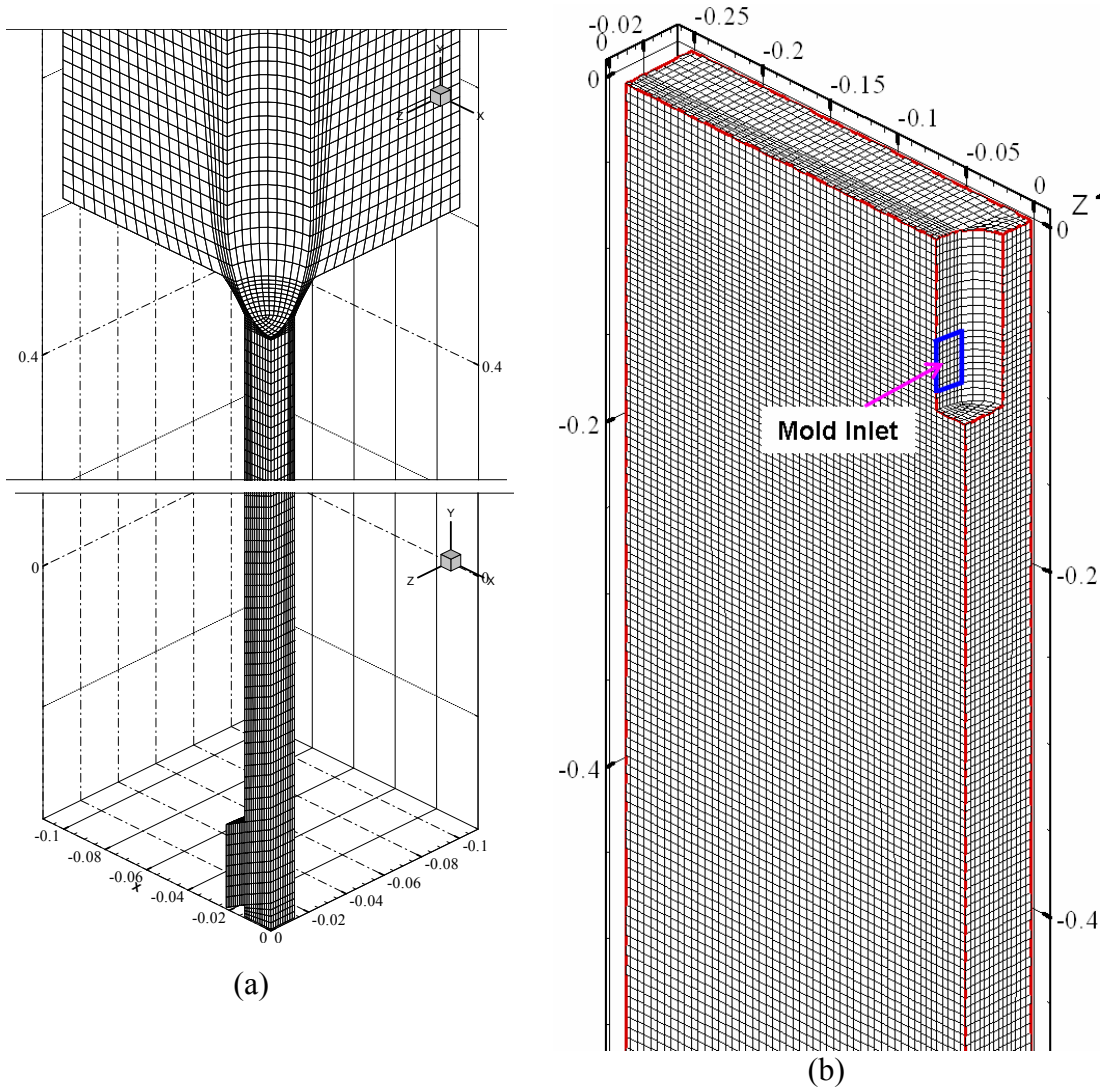

Fig-4 Isometric view of (a) well-bottom nozzle and (b) strand quarter domains and meshes

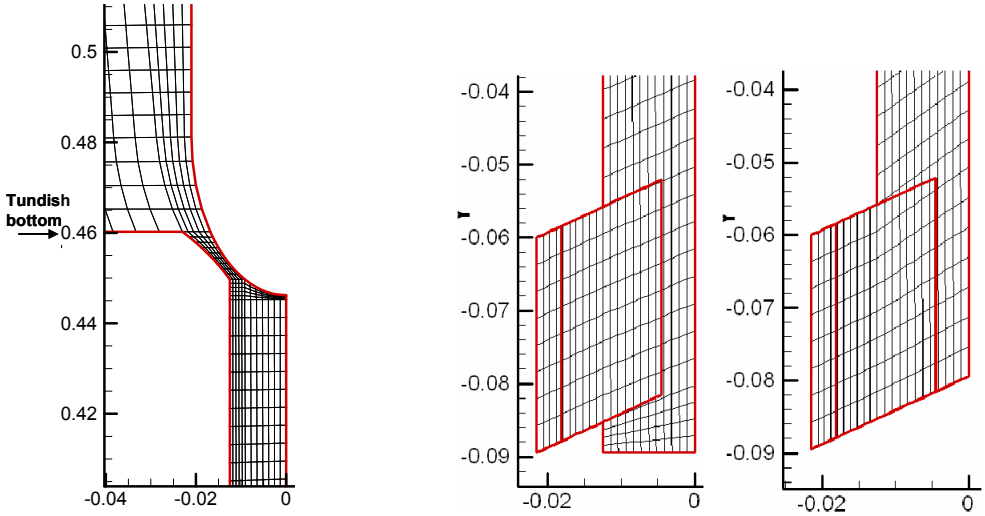

(a) (b) (c)

Fig-5 Mesh close-up in : (a) stopper-rod head region, (b) bottom region of well bottom nozzle and (c) bottom region of mountain bottom nozzle

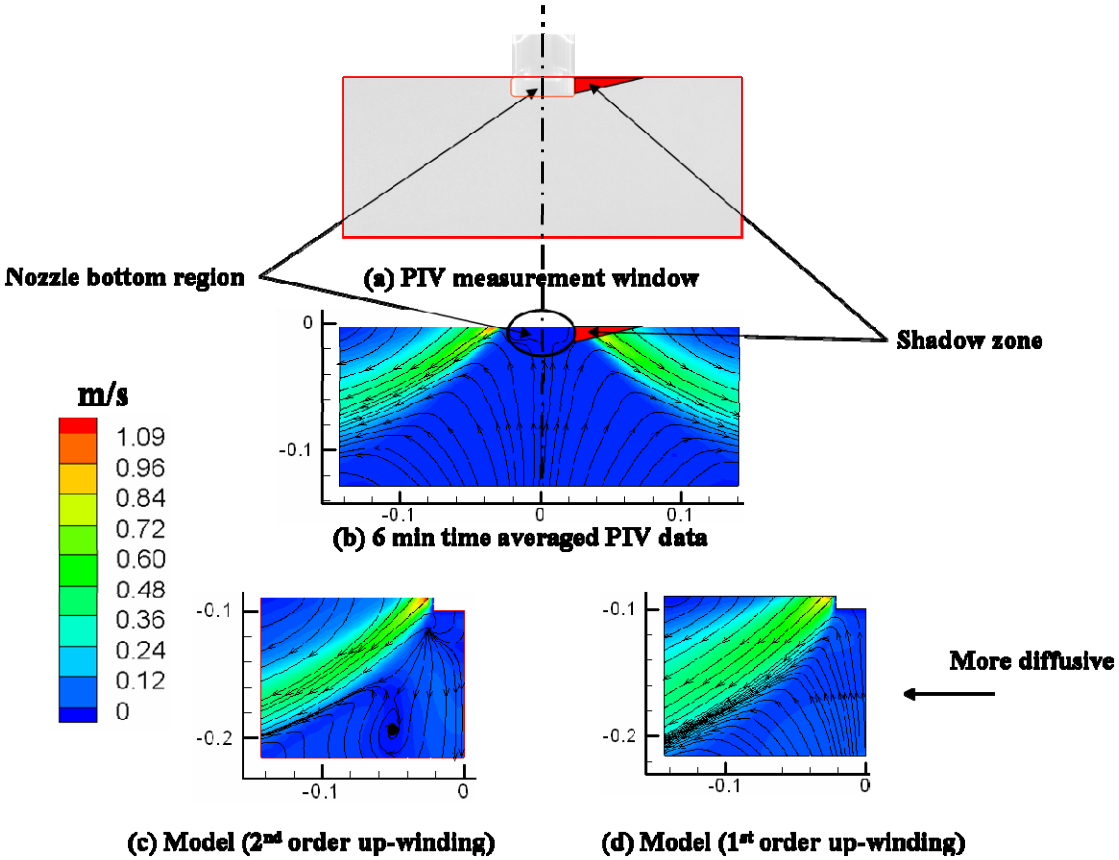

Fig-6 (a) PIV measurement window in water model with well-bottom nozzle with (b) PIV measured velocity (time-averaged over 6 min) (c) model velocity and streamlines (1st order up-wind) (d) model velocity and streamlines (2nd order up-winding)

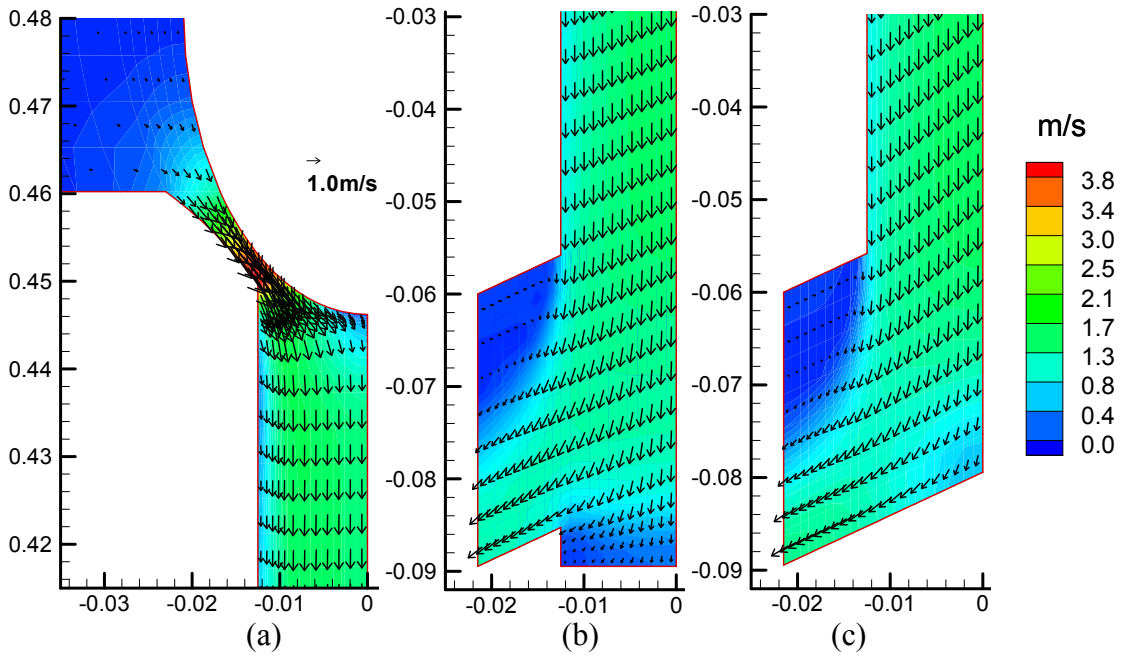

Fig-7 Comparison of velocity in (a) stopper-rod head region, (b) bottom region of well bottom nozzle and (c) bottom region of mountain bottom nozzle

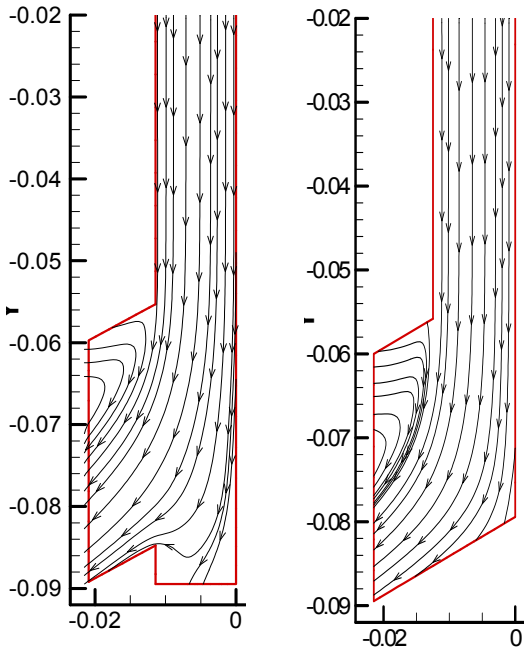

(a) (b)

Fig-8 Comparison of streamlines in (a) well and (b) mountain bottom nozzles of water model

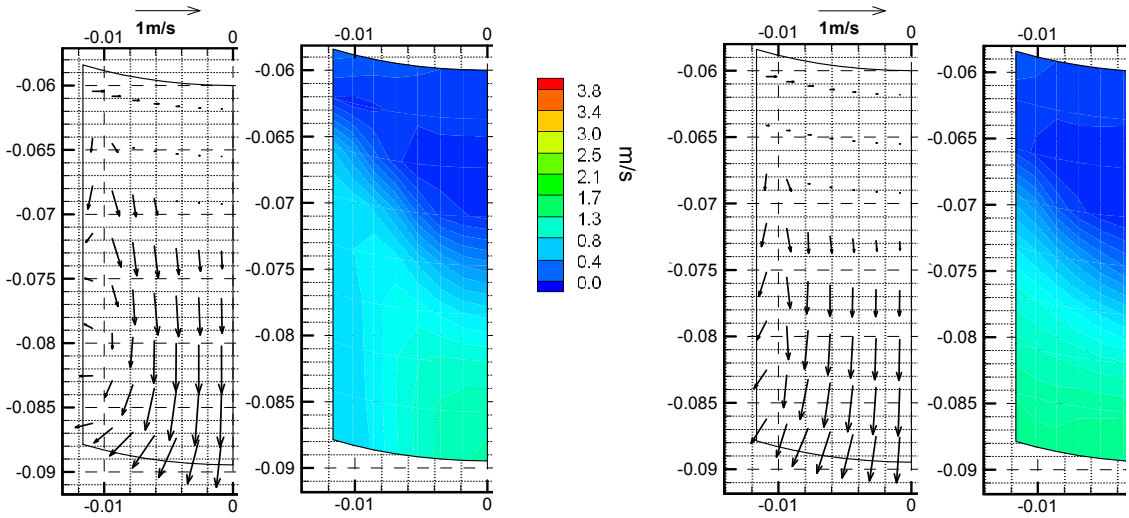

(a) well-bottom (b) mountain-bottom

Fig-9 Comparison of the port velocities

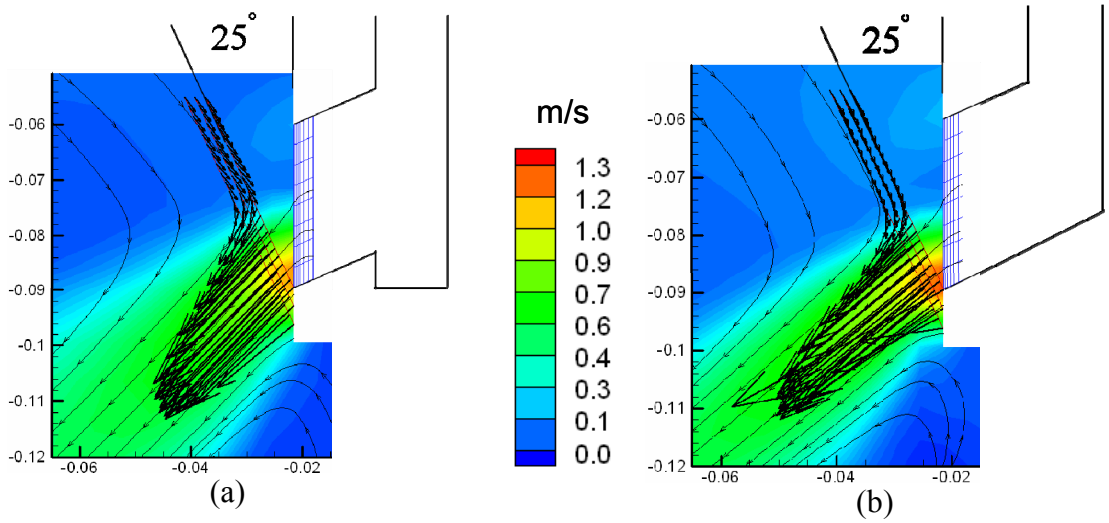

Fig-10 Calculated jet velocity vectors and speed contours near nozzle at mold centre plane in (a) well and (b) mountain bottom nozzles

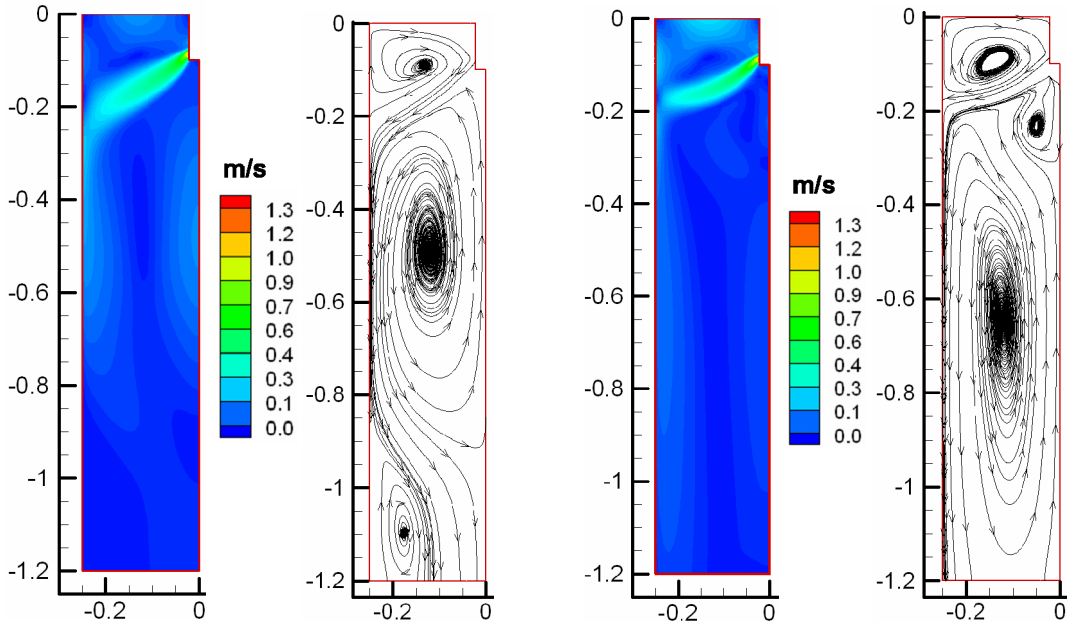

(a) (b)

Fig-11 Velocity contours and streamlines at the mid-plane between wide faces with (a) well and (b) mountain bottom nozzles in water model mold

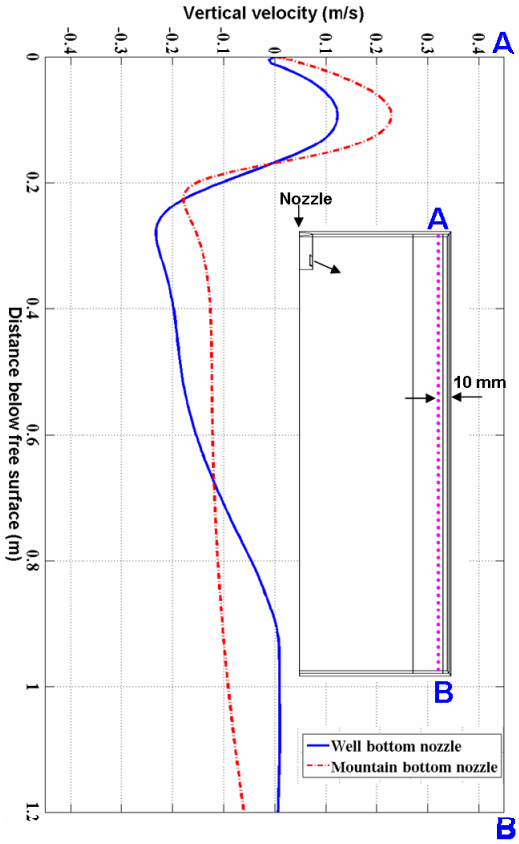

Fig-12 Vertical velocity at 10 mm from narrow face at the mid-plane between wide faces with well and mountain bottom nozzles in the water model mold

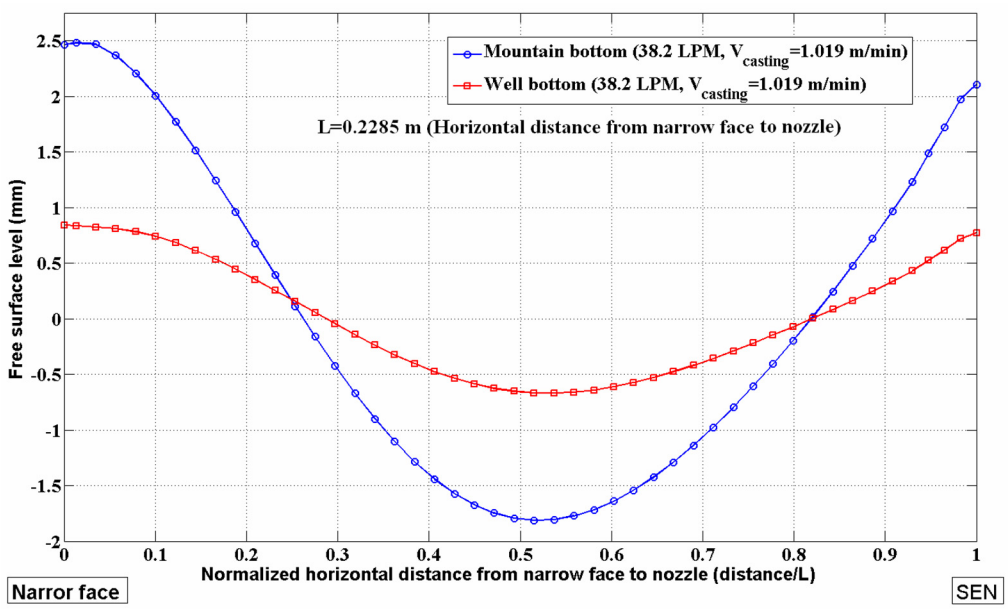

Fig-13 Free surface level comparison in well and mountain bottom nozzles of water model mold

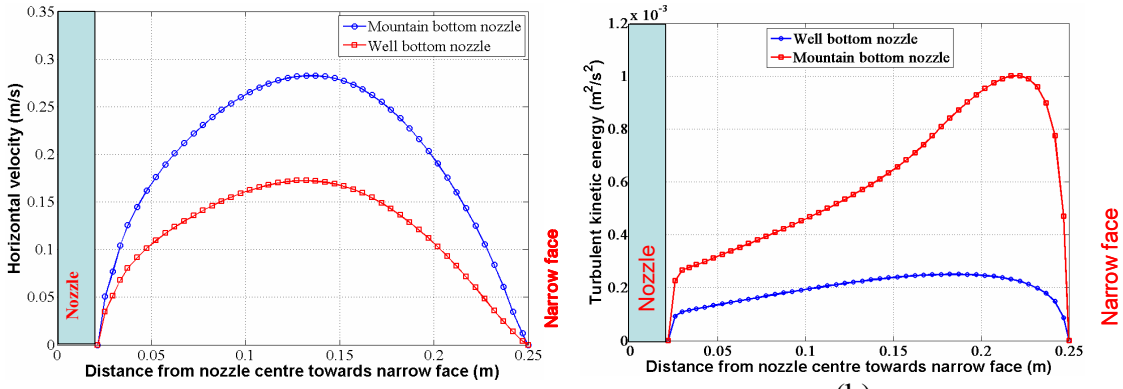

(a) (b)

Fig-14 Comparison of (a) horizontal speed and (b) turbulent kinetic energy along the centerline at the free surface in two nozzles of water model mold

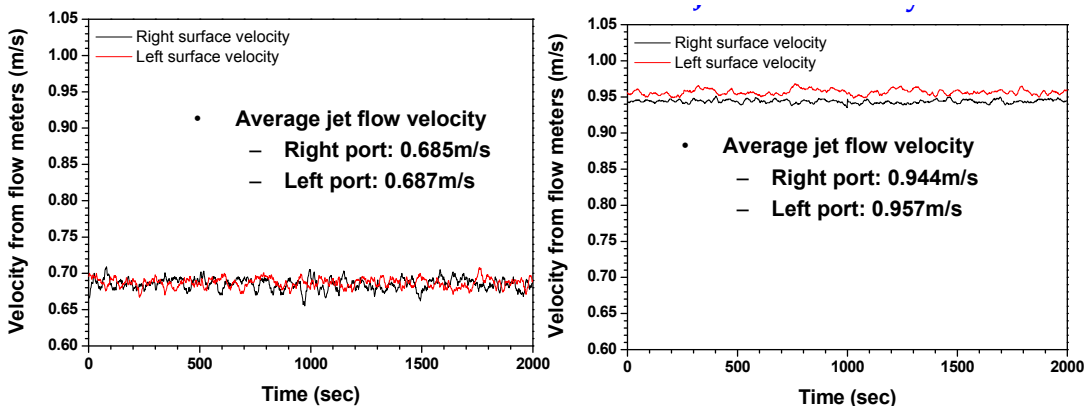

(a) (b)

Fig-15 Instantaneous jet speed measured in the water model mold with (a) well and (b) mountain bottom nozzles

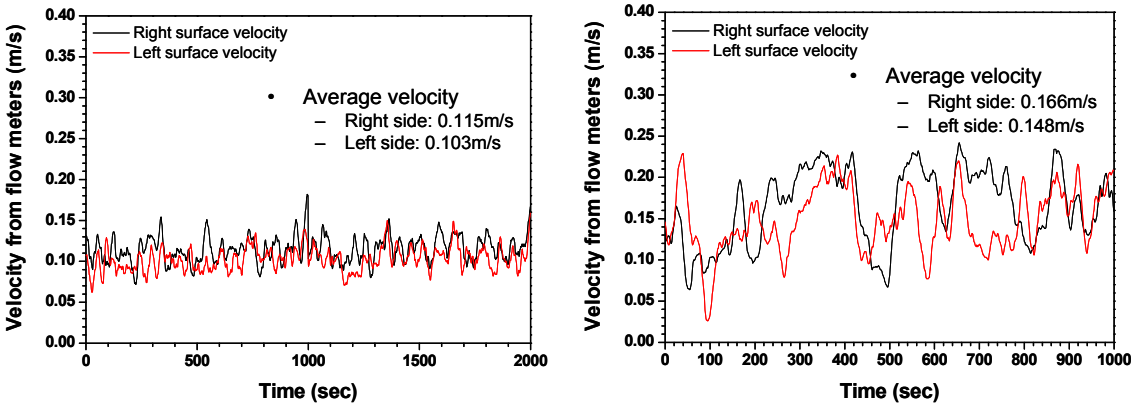

(a) (b)

Fig-16 Instantaneous surface speed measured in water model mold with (a) well bottom nozzle and (b) mountain bottom nozzle

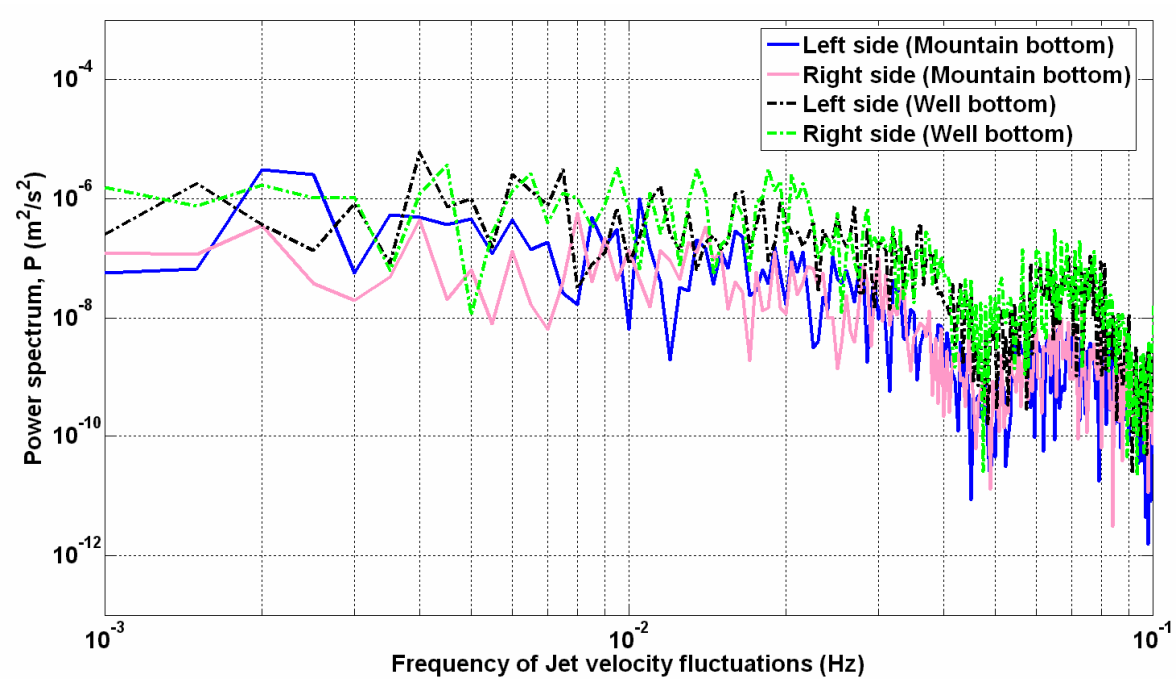

Fig-17 Power spectrum of jet velocity fluctuations measured in water model with well and mountain bottom nozzles

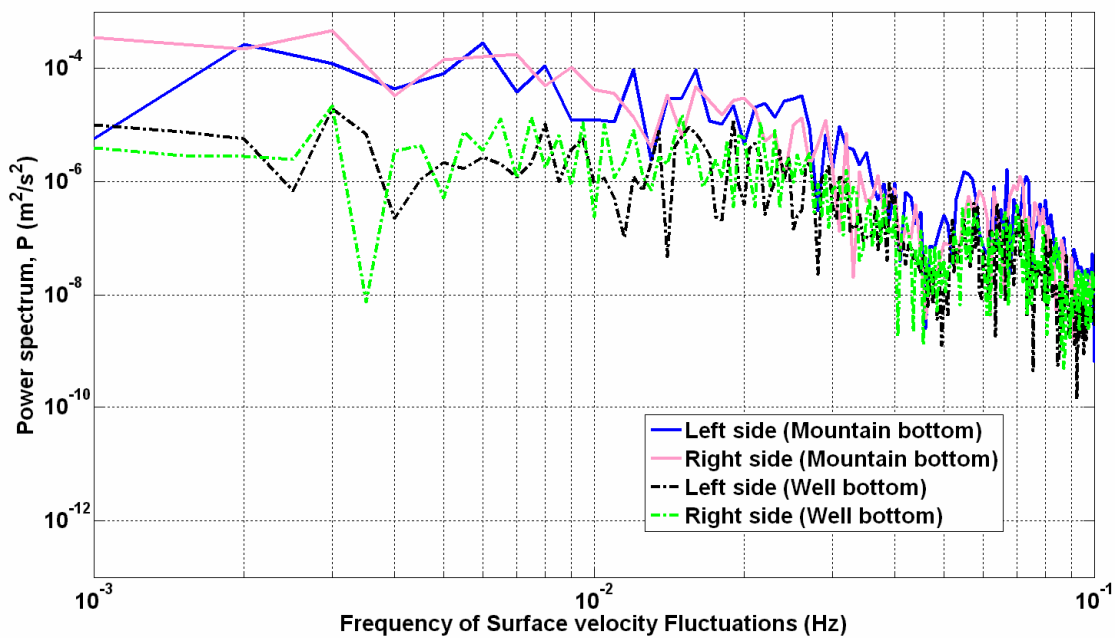

Fig-18 Power spectrum of surface velocity fluctuations measured in water model with well and mountain bottom nozzles

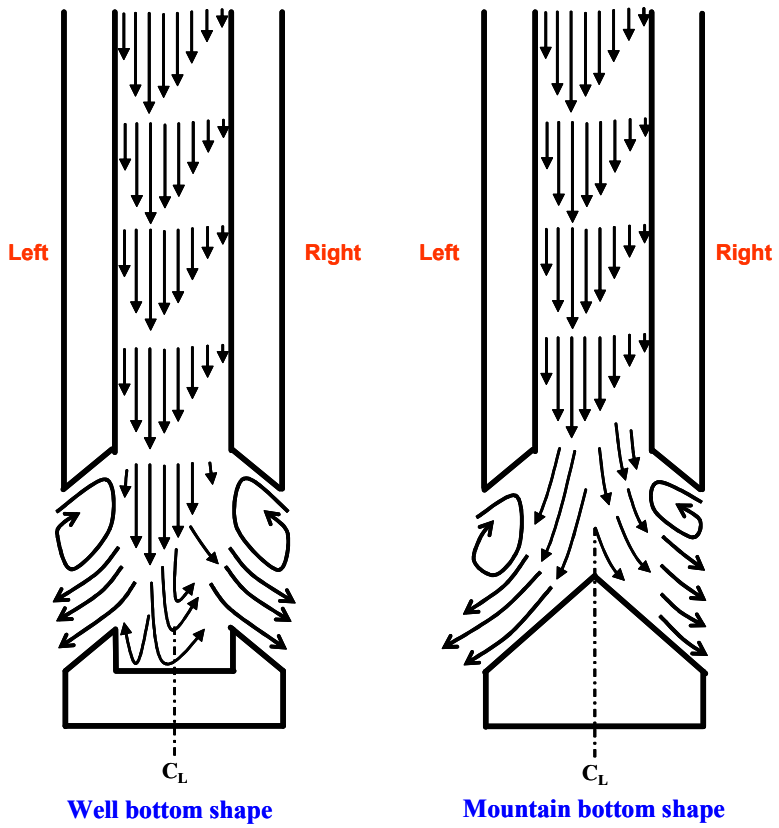

Fig-19 Schematic of effect of flow asymmetry (a) in well-bottom nozzle (b) mountain-bottom nozzle

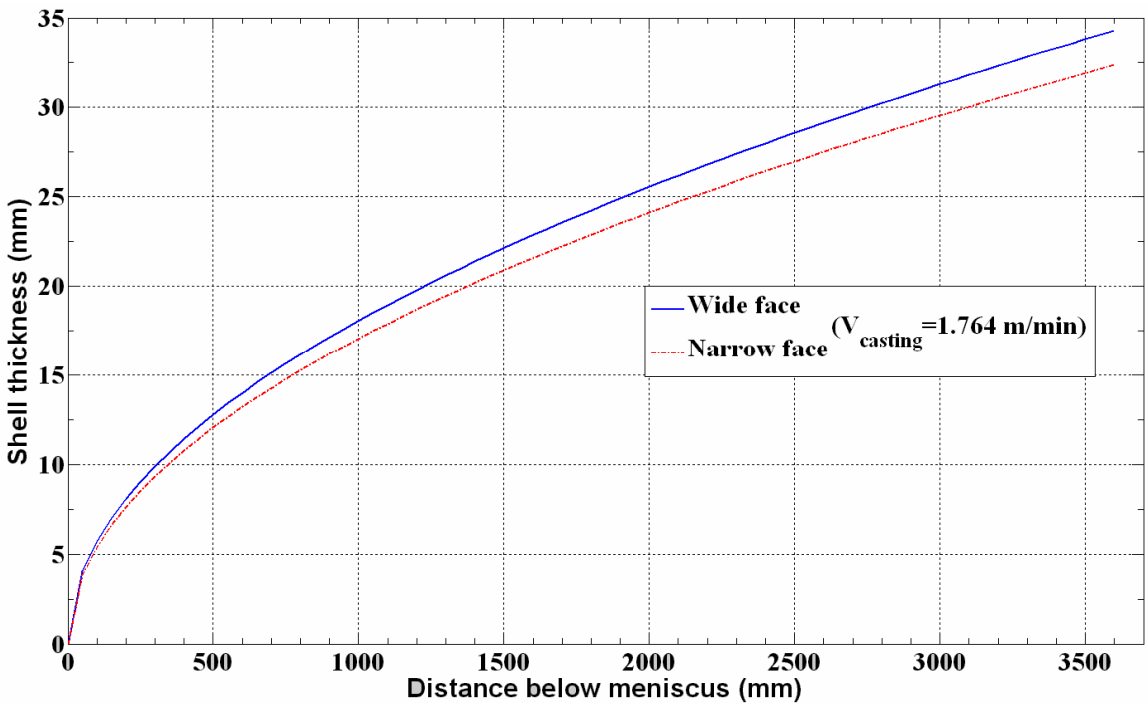

Fig-20 Shell thickness profile from CON1D

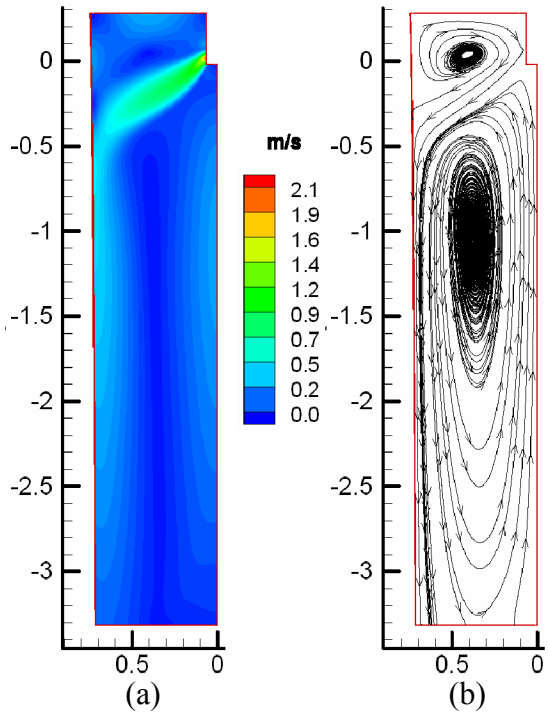

Fig-21 Velocity at mid-plane between wide faces (a) Contours and (b) Streamlines in full-scale steel caster with solidifying shell in the mold of well bottom nozzle

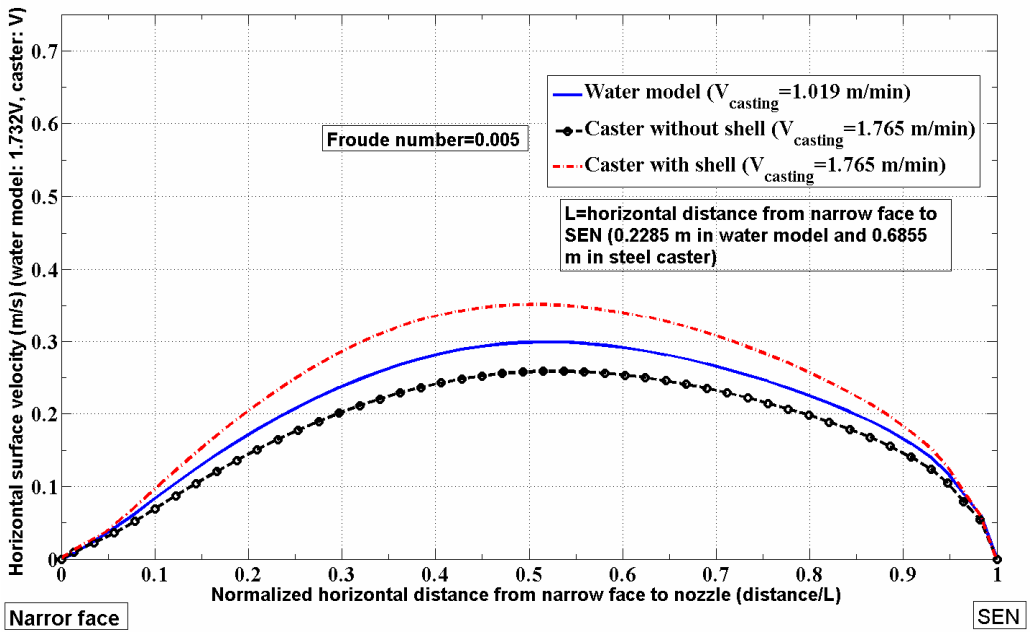

Fig-22 Comparison of surface velocities in mold of 1/3rd water model and steel caster using Froude number similarity (well bottom nozzle)

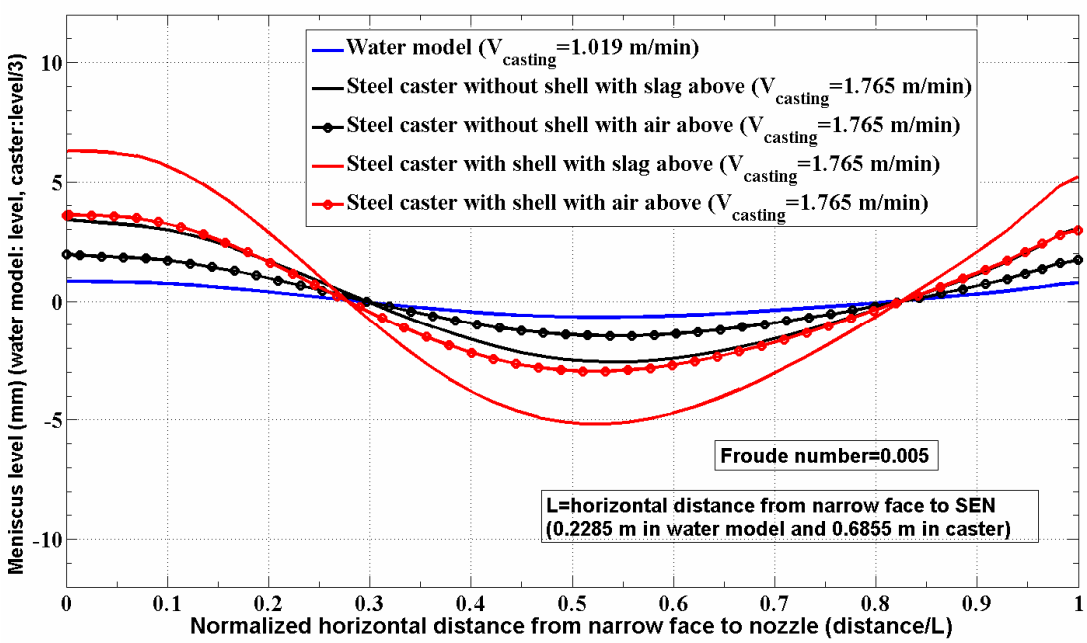

Fig-23 Comparison of liquid level in 1/3rd water model and steel caster with solidifying shell using Froude number similarity (well-bottom nozzle)

Table-1 Process parameters for experiments and computations

	Water model (1/3rd scale)	**Steel caster (full-scale)**
Stopper opening fraction	0.47	-
Nozzle port angle	25 deg down	25 deg down
Nozzle port area	23.3 mm (width) x 26.7mm (height)	69.9 mm (width) x 80.1 mm (height)
Nozzle bore diameter	25 mm	75 mm
Nozzle outer diameter	43 mm	129 mm
SEN Depth	60 mm	180 mm
Average port velocity	0.512 m/s	0.886 m/s
Fluid flow rate	38.2 LPM	595.4 LPM
Casting speed	1.02 m/min	1.76 m/min
Mold width	500 mm	1500 mm
Mold thickness	75 mm	225 mm
domain width	250 mm	750 mm
domain thickness	37.5 mm	112.5 mm (at the top)
domain length	1200 mm	3600 mm
Shell	no	Yes (see Fig-19)
Gas injection	no	no
ρ_{fluid}	998.2 kg/m^3 (water)	7020 kg/m^3 (steel)
μ_{fluid}	0.001003 kg/m-s (water)	0.006 kg/m-s (steel)
ρ_{slag}	3000 kg/m^3	

Table-2(a) Comparison of predictions and impeller measurements in jet

	Jet Velocity (m/s)			Turbulent kinetic energy(m^2/s^2) (x 10^{-3})		
	Water model		Fluent	Water model		Fluent
	Left side	Right side		Left side	Right side	
Well bottom	**0.687**	**0.685**	**0.69**	**0.0611**	**0.0898**	**22.3**
Mountain bottom	**0.957**	**0.944**	**0.92**	**0.0216**	**0.0087**	**20.1**

Table-2(b) Comparison of predictions and impeller measurements near top surface

	Horizontal Surface Velocity (m/s)			Turbulent kinetic energy(m^2/s^2) (x 10^{-3})		
	Water model		Fluent	Water model		Fluent
	Left side	Right side		Left side	Right side	
Well bottom	**0.103**	**0.115**	**0.11**	**0.31**	**0.38**	**1.4**
Mountain bottom	**0.148**	**0.166**	**0.18**	**2.23**	**3.14**	**2.4**

Table-3 Computed Jet characteristics in water model

Weighted Average Parameter	Well bottom nozzle	Mountain type nozzle
Port x-velocity (outward) (m/s)	0.75	0.92
Port y-velocity (downward) (m/s)	0.48	0.52
Port z-velocity (horizontal) (m/s)	0.065	0.076
Port turbulent kinetic energy (m^2/s^2)	0.040	0.018
Port turbulent dissipation rate (m^2/s^3)	2.11	0.64
Vertical jet downward angle (deg)	32.8	29.3
Horizontal jet angle (deg)	5.0	4.7
Average jet speed (m/s)	0.89	1.06
Back-flow zone	27%	30%

Table-4 Evaluation of well-bottom and mountain-bottom nozzle flow characteristics

	Jet velocity		Surface velocity		Asymmetry (Due to flow transients)
	Average velocity	Fluctuations	Average velocity	Fluctuations	
Well bottom	Low (Thick jet)	High (High frequency)	Low	Low (High frequency)	Low
Mountain bottom	High (Thin jet)	Low (Low frequency)	High	High (Low frequency)	High